# Chapter 4

# The GMRT Data

Recent Galactic plane observations at 843 MHz, using the Molonglo Synthesis Telescope (MOST) (Gray 1994a) and at 2.4 GHz, using the Parkes 64-m single dish (Duncan et al. 1997b), have revealed a number of new candidate SNRs. However many of these objects were in complicated regions of the Galaxy and these observations also suffered from contamination due to thermal emission at these high frequencies. Although the MOST observations were at a relatively low frequency, the side-lobes due to nearby strong sources severely limited the fidelity of images. With only single frequency data available for most of these fields (these observations did not have any overlapping fields), the identification of the candidate SNRs in these fields remained inconclusive.

A sample of candidate SNRs, accessible to the GMRT, were selected from these observations. Continuum observations of this sample were done with the GMRT at 325 MHz during the period of 1998 to 2000. The telescope hardware, on-line and off-line software were all in a state of being debugged during this period and observations were invariably intermingled with debugging activity and related observations. Consequently, the data acquired was often unusable, sometimes requiring several observing sessions involving the same field to get good data. This chapter describes the procedure used for on-line data monitoring and identification of a potential source of data corruption, off-line data flagging and finally imaging using the `AIPS` package.

Section 4.1 gives the general description of the observations done at 325 MHz. Imaging at these low frequencies requires the use of algorithms and techniques not usually used for mapping at higher frequencies. These low frequency specific problems for inversion of visibilities and image deconvolution, and the techniques used to overcome these problems are discussed in Section 4.2. Section 4.2.2 discusses the problem of bandwidth smearing of sources away from the phase centre, which necessitates the multi-channel mode of observations. The procedures used for on-line system and data monitoring are described in Section 4.3. The detailed procedure used for off-line data editing and calibration is described in Sections 4.4. Section 4.5 describes the procedure used to finally map the data and while Section 4.6 presents the full primary beam images after correcting for the primary beam attenuation.

## 4.1 GMRT Observations

325 MHz observations for continuum imaging of a sample of nine candidate SNRs were done during the period of 1998-2000. The parameters of these observations are summarized in Table 4.1. Most of the objects of interest in these fields were extended, with emission at angular scales $\sim 2-20$ arcmin requiring reliable observations at the smallest available baselines. Observations at 325 MHz are often affected by intermittent radio frequency interference (RFI) and, since RFI from nearby sources of emission remains partially correlated for the smallest baselines, data from the smallest baselines are also most severely affected by RFI. Fortunately, RFI is often narrow band and can be identified if the observing band is split into a number of narrow band frequency channels. The observations were therefore done with the full 16 MHz band split into 128 frequency channels of each having a width of $\sim 125$ kHz.

The current single side-band GMRT correlator measures only the co-polar visibilities, i.e. only signals of the same polarization are correlated using the *Indian mode* of the VLBA Multiplier and Accumulator chips (MACs). All the 128 frequency channels of the co-polar visibilities corresponding to the right and left circular polarized signals were recorded for all available baselines. The data was kept in the multi-channel format throughout the imaging process to minimize the band-width smearing of sources away from the phase centre (see Section 4.2.2). After editing the RFI-affected or otherwise bad data, a typical bandwidth of about $5-6$ MHz was finally used for imaging giving a typical RMS noise of $\sim 10$ mJy/beam.

The background sky temperature can vary by a factor of $2-3$ within the Galactic plane, resulting in a change in the total power output by similar factors. The correlator samplers are, however, optimized to work with an input signal of 0 dBm. To keep the sampler inputs at this level, *automatic level controllers* (ALCs) are introduced at the output of the baseband (BB) which effectively changes the gain to keep the output at 0 dBm. To keep

Table 4.1: Parameters of observations with GMRT

| | |
|---|---|
| Frequency of Observations (MHz) | 325 |
| RF Bandwidth (MHz) | 16 |
| Bandwidth used (MHz) | $5-6$ |
| Integration time (sec) | 16.9 |
| Average time spent on the source (hr) | 5 |
| No. of Antennas used | $20-27$ |
| Max. baseline (k$\lambda$) | $15-25$ |
| Min. baseline ($\lambda$) | $60-100$ |
| Max. spatial scale(arcmin) | $\sim 30$ |
| Average Antenna Sensitivity (K/Jy) | 0.32 |
| Primary beam (degree) | 1.4 |
| Synthesized resolution (arcsec) | $10-20$ |
| RMS noise (mJy/beam) | $\sim 10$ |

the ALC operating point within its linear operating range, an attenuation of 16 db was typically used for the IF and BB signals.

As mentioned earlier, the GMRT was in a state of being debugged during the period of the observations. Consequently, the number of antennas and the longest baseline available changed from observation to observation. As a result, the resolution changes from observation to observation. However, most of the *Central Square* antennas, plus some of the arm antennas were available for all observations giving angular resolution in the range $\approx 60-10$ arcsec. Some of the fields, which needed higher resolution were observed when the long baselines antennas were available. Since most of the target objects were extended, it was essential that the short antenna spacings were well sampled. Hence the three antennas, C05, C06 and C09 which provide the shortest spacings, were used for all observations giving a shortest baseline of $\sim 100\lambda$ (after flagging bad data) for which reliable data was measured. This corresponds to a largest angular scale of $\sim 30$ arcmin. Most of the sources of interest were well within this limit in angular size and we believe that most of the emission up to angular scales of $\sim 30$ arcmin is well represented in the GMRT 325-MHz images.

## 4.2 Low frequency specific problems

The visibility measured by a properly calibrated interferometer is given by

$$V(u,v,w) = \iint I(l,m)P(l,m)e^{-2\pi\iota(ul+vm+w(\sqrt{1-l^2-m^2}-1))}\frac{dldm}{\sqrt{1-l^2-m^2}} \quad (4.1)$$

where $(u,v,w)$ are the antenna co-ordinates in the $uvw$ co-ordinate system, $l, m$, and $n$ are the direction cosines in this system, $I(l,m)$ is the source brightness distribution (the image) and $P(l,m)$ is the far field antenna reception pattern (the primary beam). For further analysis we will assume $P=1$, and drop it from all equations (for typing convenience!), remembering all along that the effect of $P(l,m)$ is to limit the part of sky from which the antenna can receive radiation to $\sim \lambda/D$ radians, where $D$ is the diameter of the antennas.

For a small field of view ($l^2+m^2 << 1$), the above equation can be approximated well by a 2D Fourier transform relation. The other case in which this is an exact 2D relation is when the antennas are perfect aligned along the East-West direction. Here, we discuss the problem of mapping with non-East-West arrays. The derivation presented here of results for devising algorithms used for imaging large fields of view presented here follow the treatment of Cornwell & Perley (1992) and Cornwell & Perley (1999).

### 4.2.1 Mapping with non co-planar arrays

Equation 4.1 also reduces to a 2D relation for a non-East-West array, if the integration time is sufficiently small (snapshot observations). However modern arrays are designed to maximize the *uv-coverage* with the antennas arranged in a 'Y' shaped configuration (non East-West arrays) (Mathur 1969). Fields, such as the ones observed for this dissertation, with emission at all angular scales, require maximal uv-coverage. Telescopes such as the GMRT use the rotation of earth to improve the uv-coverage and observations of complex fields typically last for several hours. Hence, Equation 4.1 needs to be used to map the full primary beam of the antennas, particularly at low frequencies.

Let $n=\sqrt{1-l^2-m^2}$ be treated as an independent variable. A 3D Fourier transform of $V(u,v,w)$ can be written using $(u,v,w)$ and $(l,m,n)$ as a set of conjugate variables as

$$F(l,m,n) = \iiint V(u,v,w)e^{2\pi\iota(ul+vm+wn)}dudvdw \quad (4.2)$$

Substituting for $V(u,v,w)$ from Equation 4.1 we get

$$
\begin{aligned}
F(l,m,n) = \iint \Bigg\{ \quad & \frac{I(l',m')}{\sqrt{1-l'^2-m'^2}} \\
& \iiint e^{-2\pi\iota(u(l'-l)+v(m'-m)+w(\sqrt{1-l'^2-m'^2}-n-1))} du dv dw \\
\Bigg\} \quad & dl' dm'
\end{aligned} \tag{4.3}
$$

The $-1$ in the coefficient of $w$ in Equation 4.1 comes from fringe rotation. In the above equation, it corresponds to a shift by one unit along the $n-$axis. Since this is only a change of the origin of the co-ordinates system, it can be absorbed in the $n$ without loss of generality. Using the general result

$$
\begin{aligned}
\delta(l'-l) &= \int e^{-2\pi\iota u(l'-l)} du \\
&= \begin{cases} 1 & : \quad l = l' \\ 0 & : \quad otherwise \end{cases}
\end{aligned} \tag{4.4}
$$

we get

$$
\begin{aligned}
F(l,m,n) &= \iint \frac{I(l',m')}{\sqrt{1-l'^2-m'^2}} \delta(l'-l)\delta(m'-m)\delta(\sqrt{1-l'^2-m'^2}-n) dl' dm' \\
&= \frac{I(l,m)\delta(\sqrt{1-l^2-m^2}-n)}{\sqrt{1-l^2-m^2}}
\end{aligned} \tag{4.5}
$$

This equation then provides the connection between the 2D sky brightness distribution given by $I(l,m)$ and the result of a 3D Fourier inversion of $V(u,v,w)$ given by $F(l,m,n)$ referred to as the *Image volume*. Here after, I use $I(l,m,n)$ to refer to this *Image volume*.

The effect of including the fringe rotation term $(-2\pi w)$ would be a shift of the *Image volume* by one unit in the conjugate axis ($n-$axis) (shift theorem of Fourier transforms; Bracewell 1986 [and later eds]). Hence, the effect of fringe stopping is to make the $lm-$plane coincide with the tangent plane at the phase center on the Celestial sphere (the point where the tangent plane touches the Celestial sphere) with the rest of the sphere completely contained inside the *Image volume* (Fig. 4.1).

Noting that the third variable $n$ of the *Image volume* is not an independent variable and is constrained to be $n = \sqrt{1-l^2-m^2}$, Equation 4.5 gives the physical interpretation of $I(l,m,n)$. Imagine the Celestial sphere defined by $l^2+m^2+n^2 = 1$ enclosed by the *Image volume* $I(l,m,n)$, with the top most plane being tangent to the Celestial sphere as

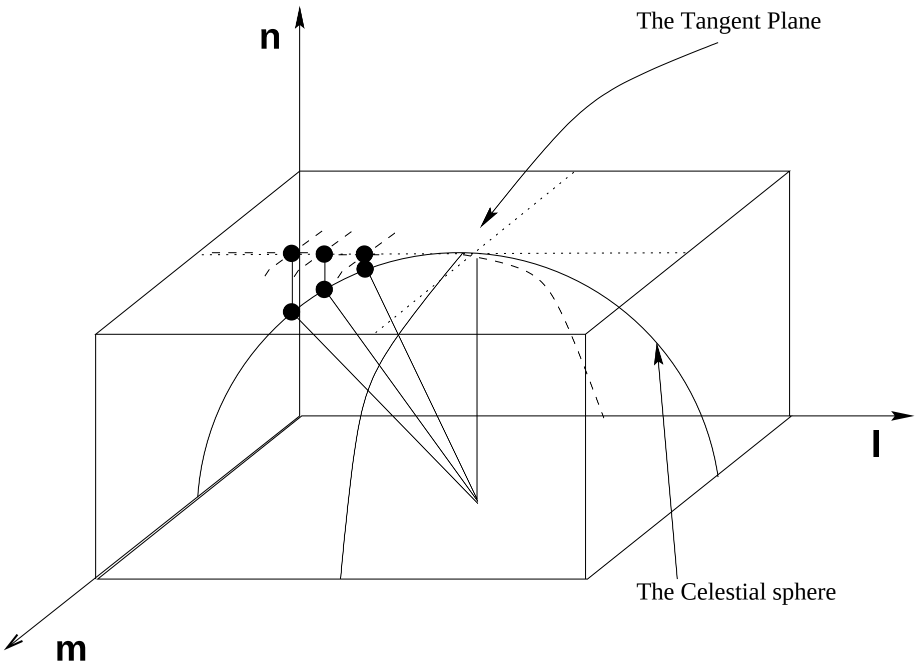


Figure 4.1: Graphical representation of the geometry of the *Image volume* and the Celestial sphere. The point at which the Celestial sphere touches the first plane of the *Image volume* is the point around which the 2D image inversion approximation is valid. For wider fields, emission at points along the intersection of Celestial sphere and the various planes (labeled here as the Celestial Sphere) needs to be projected to the tangent plane to recover the undistorted 2D image. This is shown for 3 points on the Celestial sphere, projected on the tangent plane.

shown in Fig. 4.1. Equation 4.5 then tells that only those parts of the *Image volume* correspond to the physical emission which lie on the surface of the Celestial sphere. However, the *Image volume* will be convolved by the telescope transfer function. The telescope transfer function is the Fourier transform of the sampling function $S$ in the $uvw$ frame (see Chapter 2, page 48). The telescope transfer function, referred to as the *dirty beam* and defined as $B(l,m,n) = \mathcal{FT}[S(u,v,w)]$, also defines a volume in the image domain. The *dirty image volume* defined by the relation $I^d(l,m,n) = I(l,m,n) \star B(l,m,n)$ is a convolution of $I(l,m,n)$ with $B(l,m,n)$. Since the *dirty beam* is not constrained to be finite only on the Celestial sphere, $I^d$ will be finite away from the surface of the Celestial sphere corresponding to non-physical emission due to the side lobes of $B(l,m,n)$. A 3D deconvolution using the *dirty image* and the *dirty beam volumes* will produce a *Clean image volume*. An extra operation of projecting all points in the *CLEAN image-volume* along

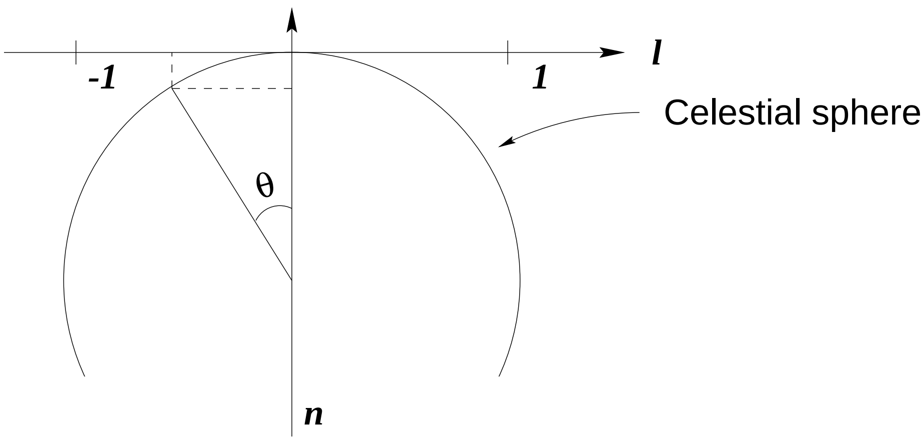


Figure 4.2: Graphical illustration to compute the distance between the tangent plane and a point in the sky at an angle of $\theta$.

the Celestial sphere onto the 2D tangent plane to recover the 2D sky brightness distribution is therefore required. Graphical representation of the geometry for this is shown in Fig. 4.1.

### 3D imaging

The most straight forward method suggested by Equation 4.5 for recovering the sky brightness distribution, is to perform a 3D Fourier transform of $V(u, v, w)$. This requires that the $w$ axis be also sampled at the Nyquist rate (Bracewell 1986 [and later eds]; Brigham 1988 [and later eds])). For most observations, it turns out that this is rarely satisfied and doing a FFT along the third axis would result into severe aliasing. Therefore, in practice, the Fourier transform on the third axis is usually performed using the direct Fourier transform (DFT) on the un-gridded data.

To perform the 3D FT (FFT along the $u-$ and $v-$ axis and DFT along the $w-$axis) one still needs to know the number of planes needed along the $n-$axis. This can be found using the geometry shown in Fig. 4.2. The size of the synthesized beam along the $n-$axis is comparable to that along the other two directions and is given by $\approx \lambda/B_{max}$ where, $B_{max}$ is the longest projected baseline length. The separation between the planes along $n$ should be $\leq \lambda/2B_{max}$. The distance between the tangent plane and a point separated by $\theta$ from the phase center, for small values of $\theta$, is given by $1-\cos(\theta) \approx \theta^2/2$. For a field of view of angular size $\theta$, critical sampling would be ensured if the number of planes along the $n-$axis, $N_n$, is

$$\begin{aligned} N_n =& B_{max}\theta^2/\lambda \\ =& \lambda B_{max}/D^2 \text{ (for } \theta = \text{Full Primary beam)} \end{aligned} \tag{4.6}$$

where $D$ is the diameter of the antenna ($B_{max} \approx 25$ km for the GMRT at 325 MHz). Therefore, for mapping a $1^\circ$ field of view without distortions, one would require 8 planes along the $n$-axis. However, for mapping with *Central Square* alone ($B_{max} \approx 1$ km), one plane is sufficient. At these frequencies, it becomes important to map most of the primary beam since the number and often the intensity of the sources in the field increase and the side-lobes due to these sources limit the dynamic range in the maps. Hence, even if the source of interest is small, it requires a full 3D inversion (and deconvolution).

Another reason why more than one plane would be required for very high dynamic range imaging is as follows. Strictly speaking, the only point which lies in the tangent plane is the point at which the tangent plane touches the Celestial sphere. All other points in the image, even close to the phase center, lie slightly below the tangent plane. Deconvolution of the tangent plane then results into distortions for the same reason as the distortions due to the deconvolution of a point source which lies between two pixels in the 2D case (Briggs 1995). As in the 2D case, this problem can be minimized by over sampling the image which, in this case, implies having more than one plane along the $n$-axis, even if Equation 4.6 implies that one plane is sufficient.

**Polyhedron imaging**

As mentioned above, emission from the phase center and from points close to it, lie approximately in the tangent plane. Polyhedron imaging relies on exploiting this by approximating the Celestial sphere by a number of tangent planes, referred to as facets, as shown in Fig. 4.3. The visibilities are recomputed to shift the phase center to the tangent points of each facet and a small region around each of the tangent points is then mapped using the 2D approximation.

The number of planes required to map an object of size $\theta$ can be found simply by requiring that the maximum separation between the tangent plane and the Celestial sphere be less than $\lambda/B_{max}$, the size of the synthesized beam. As shown earlier, this separation for a point $\theta$ degrees away from the tangent point is $\approx \theta^2/2$. Hence, for critical sampling,

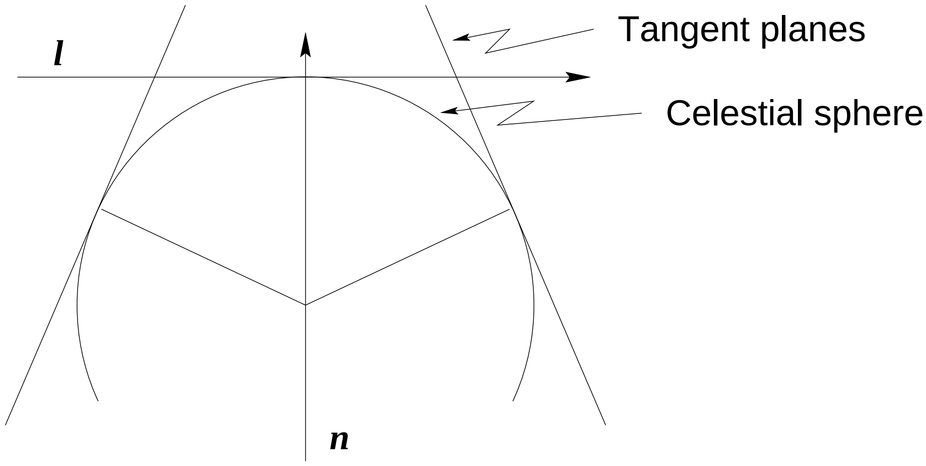


Figure 4.3: Approximation of the Celestial sphere by multiple tangent planes (polyhedron imaging).

the number of planes required is equal to the solid angle subtended by the sky being mapped ($\theta_f^2$) divided by $\theta^2/2 (= \lambda/2B_{max})$

$$\begin{aligned} N_{poly} &= 2\theta_f^2 B_{max}/\lambda \\ &= 2B_{max}\lambda/D^2 \;\; (\text{for } \theta_\mathrm{f} \;=\; \text{Full primary beam}) \end{aligned} \tag{4.7}$$

Notice that the number of planes required is twice as many as required for 3D inversion. However, since a small portion around the tangent point of each plane is used, the size of each of these planes can be small, off-setting the increase in computations due to the increase in the number of planes required. Another approach which is often taken for very high dynamic range imaging, is to do a full 3D imaging on each of the planes. This would effectively increase the size of the field that can be imaged on each tangent plane, thereby reducing the number of planes required.

The polyhedron imaging scheme is implemented in the current version of the `AIPS` data reduction package and the 3D inversion (and deconvolution) is implemented in the (no longer supported) `SDE` package developed by T.J. Cornwell et al. Both these schemes, in their full glory, are available in the (recently released) `AIPS++` package.

The GMRT 325-MHz data was imaged using the `IMAGR` task in `AIPS`. This program implements the polyhedron algorithm and requires the user to supply the number of facets to be used and a list of the locations of the centre of each facet with respect to the image centre and the size of each facet. This list of facets and their parameters were computed using the task SETFC in AIPS, typically resulting in a grid of $5 \times 5$ facets, each of size $256 \times 256$ pixels.

### 4.2.2 Bandwidth Smearing

The effect of a finite bandwidth of observation as seen by the multiplier in the correlator, is to reduce the amplitude of the visibility by a factor given by $\frac{sin(\pi l \Delta\nu/\nu_o \theta)}{(\pi l \Delta\nu/\nu_o \theta)}$ where $\theta$ is the angular size of the synthesized beam, $\nu_o$ is the center of the observing band, $l$ is location of the point source relative to the field center and $\Delta\nu$ is the bandwidth of the signal being correlated.

The distortion in the map due to the finite bandwidth of observation can be understood as follows. For continuum observations, the visibility data integrated over the bandwidth $\Delta\nu$ is treated as if the the observations were made at a single frequency $\nu_o$ – the central frequency of the band. As a result the $u$ and $v$ co-ordinates and the value of visibilities are correct *only* for $\nu_o$. The true co-ordinates at other frequencies in the band are related to the recorded co-ordinates as

$$(u, v) = \left(\nu_o \frac{u_\nu}{\nu}, \nu_o \frac{v_\nu}{\nu}\right) \tag{4.8}$$

Since the total weights $W$, used while mapping, does not depend on the frequency, the relation between the brightness distribution and visibility at a frequency $\nu$ becomes

$$V(u, v) = V\left(u_\nu \frac{\nu_o}{\nu}, v_\nu \frac{\nu_o}{\nu}\right) \mathcal{FT} \left(\frac{\nu}{\nu_o}\right)^2 I\left(l\frac{\nu}{\nu_0}, m\frac{\nu}{\nu_0}\right) \tag{4.9}$$

Hence the contribution of $V(u, v)$ to the brightness distribution get scaled by $(\nu/\nu_o)^2$ and the co-ordinates get scaled by $(\nu/\nu_o)$. The effect of the scaling of the co-ordinates, assuming a delta function for the *Dirty Beam*, is to smear a point source at position $(l, m)$ into a line of length $(\Delta\nu/\nu_o)\sqrt{l^2 + m^2}$ in the radial direction. This will get convolved with the *Dirty Beam* and the total effect can be found by integrating the brightness distribution over the bandwidth as given in Equation 4.9

$$I^d(l, m) = \left[\frac{\int\limits_0^\infty |H_{RF}(\nu)|^2 \left(\frac{\nu}{\nu_o}\right)^2 I\left(\frac{l\nu}{\nu_0}, \frac{m\nu}{\nu_0}\right) d\nu}{\int\limits_0^\infty |H_{RF}(\nu)|^2 d\nu}\right] * DB_o(l, m) \tag{4.10}$$

where $H_{RF}(\nu)$ is the band-shape function of the RF band and $DB_o$ is the *Dirty Beam* at frequency $\nu_o$. If the synthesized beam is represented by a Gaussian of standard deviation $\sigma_b = \theta_b/\sqrt{8\ln 2}$ and the bandpass by a rectangular function of width $\Delta\nu$, the fractional reduction in the strength of a source located at a radial distance of $r = \sqrt{l^2 + m^2}$ is given by

$$R_b = 1.064 \frac{\theta_b \nu_o}{r \Delta\nu} \mathrm{erf}\left(0.833 \frac{r\Delta\nu}{\theta_b \nu_o}\right) \tag{4.11}$$

Equation 4.10 is equivalent to averaging a large number of maps made from quasi-monochromatic visibilities at $\nu$. Since each such map scales by a different factor, a source away from the center would move along the radial line from one map to another, producing the radial smearing mentioned above, convolved with the *Dirty Beam*.

The effect of bandwidth smearing can be reduced if the band is split into frequency channels with smaller channel widths. This effectively reduces the bandwidth $\Delta\nu$ as seen by the mapping procedure and while gridding the visibilities, $u$ and $v$ can be computed separately for each channel and assigned to the appropriate uv-cell. The FX correlator used in GMRT provides up to 128 frequency channels over the entire bandwidth of observation and the visibilities can be retained as multi-channel in the mapping process to reduce bandwidth smearing. Although purely from the point of view of bandwidth smearing, averaging $\sim 10$ channels at 325 MHz would be acceptable, keeping the visibility database with all the 128 channels is usually recommended to allow identification and flagging of narrow bands RFI.

## 4.3 Observational procedure

For $T^a \ll T^{sys}$, the amplitude of the visibility function $V$ is proportional to the flux density of the source and the normalized visibility amplitude is converted to flux density units using the measurement of $V$ for a source of known but non variable flux density (referred to as the flux density calibrator). Also, the complex antenna based gain can potentially vary as a function of time. These slow time variations can be corrected using periodic observation of a source of known structure, usually an unresolved source, referred to as the phase calibrator. The flux density of the phase calibrators, the flux density of which is potentially variable over time scales of days, is also calibrated using the flux density calibrator. Each observation therefore requires at least one observation of a flux density calibrator and periodic observation of phase calibrators to properly calibrate the data.

The VLA flux density calibrators, `3C48` and `3C286` was used for all observations. One of three calibrators close to the Galactic plane namely, `1830-36`, `1709-299` and `1822-096`, were used as the phase calibrator. A flux calibrator was observed for $\sim 10$ min at the beginning and at the end of each observing session and the phase calibrator was observed for $\sim 10$ min at an intervals of $\sim 30$ min.

The planned periodic injection of noise from a calibrated noise source to measure the system temperature has not yet been implemented for the GMRT. As a result, the system temperatures for the flux density calibrator fields ($T^{sys}_{Cal}$) and the field being mapped ($T^{sys}_{s}$) must be measured and a correction equal to $T^{sys}_{s}/T^{sys}_{Cal}$ be applied as part of the flux density calibration. $T^{sys}_{Cal}$ was measured to be $\sim 110$ K while $T^{sys}_{s}$ was estimated from the all-sky maps at 408 MHz (Haslam et al. 1981, 1982, 1995). For a few fields, $T^{sys}_{s}$ was also measured at few points around the source of interest and the measured system temperature was consistent with that estimated from the 408 MHz data to within $\sim 10\%$. None of the phase calibrators used for these observations are known to be variable over few hours. These calibrators were therefore also used as secondary amplitude calibrators to effectively correct for any slow variation in the receiver temperature.

The observing schedule if the GMRT on-line array control system can be supplied via a computer readable file. This file, apart from a few other system-related commands, contain instructions about the source to be tracked and the integration time on each source. However since the feedback of the antenna pointing status is not used, this file needs to be tweaked by inserting delays between various commands. For example, the amount of time taken for antennas to move from one tracking direction to another varies from antenna to antenna, and appropriate time delays must be inserted between the various commands in this file to make sure that the data recording begins only after *all* antennas have reached a given tracking position. The commands for alternately tracking the phase calibrator and the target source were put in an infinite loop, which allowed the above mentioned periodic observations of the phase calibrator. However, since only an infinite loop is possible, the observations had to be manually terminated at the end of observing session. Information about the status of the antennas as well as a mechanism to derive time-of-the-day information in the command syntax used in this file is highly desirable and will allow a better and more automated observing session.

### 4.3.1 On-line monitoring

The data could be corrupted due to a number of reasons including (1) RFI, (2) catastrophic hardware failures (irrecoverable in a short time), (3) intermittent hardware failures from which a quick recovery is possible (e.g. breakdown of communication between correlator control hardware and software), (4) antenna-based breakdown (for e.g., failure of the servo system resulting in stoppage of source tracking), (5) failure of the communication link between the antenna based computer (ABC) and the on-line control computer at the CEB, (6) power supply failure to some of the antennas, (7) loss of phase-lock for the four local oscillators (LOs) or a phase jump in the LOs, (8) onset of ionospheric scintillations, (9) problems in the online array control, (10) problems in the correlator control software/hardware, etc. Data affected by any or many of these sources manifests itself in various forms in the recorded data. Such data needs to be flagged from the database before it is used for mapping. The flagging information for the database was generated by on-line monitoring of the critical array control parameters as well by off-line examination of the data itself. The procedure used for this is described below.

#### System monitoring

It was noticed that problems related to items (3), (4), (5) and (10) listed above, occurred frequently enough to require careful monitoring of various related telescope parameters as well as on-line monitoring of the visibility data. The GMRT on-line array control system maintains a large amount of information about the status of the various subsystems. This information is updated once every few seconds and is available in the shared memory resource of the control computer. Any arbitrary information from this resource can be extracted using the `table`[1] program. This program was used to extract the following information as a function of time:

- the packet sequence number
- the azimuth and elevation angles of the antennas
- the error between the target and current antenna azimuth and elevation angles
- the antenna servo system related flags

The `table` program produces the output in the form of a table which was supplied to a shell script which generated an alarm if any of the following conditions occurred:

[1]Developed by R.K.Singh of NCRA(TIFR), Pune

- the error on azimuth or elevation angles of any of the antennas exceeded a threshold value. This usually was an indication of the antenna not receiving the the periodic tracking instructions from the GMRT on-line array control system computer

- the packet sequence number did not change for a threshold length of time. This usually indicated loss of communication between the antennas and the GMRT online array control system computer

- the flag for servo brakes was raised for any of the antennas. This usually indicated either a malfunctioning antenna servo system and/or the detection of extra antenna load (due to wind loading or due to some spurious signal indicating extra load)

In case of any of the above problems, manual intervention was required. However, this rather primitive "automation" did help enormously in long observing sessions. This procedure, while already quite useful, should ultimately be made part of the link between the GMRT on-line array control system and the correlator control software to (1) record on-line flagging information, and (2) control the recording of the data.

**Data monitoring**

On-line monitoring of the visibility data was done in two ways. First, the `matmon`[2] program was used to monitor the normalized correlation coefficient for the phase calibrators. This program displays single integration cycle snapshots of the amplitude (or the phase) of the visibility data for all baselines in the form of a matrix. This display was used to determine the general health of the system before starting the observations and was useful in quickly locating catastrophic problems. Once the observations were started, the data from the correlator was monitored using the programs `xtract`, `rantsol` and `closure` (see Chapter 3). The amplitude and phase from all baselines were continuously displayed as a set of stacked scrolling line plots using the program `oddix` (which uses `xtract` and the plotting package of the GMRT off-line software). This display provided a $1-2$ hour long snapshot of the data covering two or more observations of the phase calibrator. Since most problems in the system can be detected using the data from the phase calibrators, the onset of a problem in the data between two calibrator scans was easily detected using these plots.

[2]Developed by A.P.Rao of NCRA(TIFR), Pune

The output of `rantsol` (namely, the antenna based complex gains) for the calibrator scans was also similarly plotted. These plots provided information about the health of the system containing all the data on the calibrator scans. Problems ranging from a significant loss in antenna sensitivity (e.g. due to change in the antenna pointing offset across $HA = 0$h seen for some of the antennas) to the onset of closure errors due to a malfunctioning correlator or the onset of ionospheric scintillations were quickly detected from these plots.

The output of `closure` (the closure phase for all possible triangles) was supplied to another program which raised an alarm if the closure phases exceeded a threshold value for a threshold length of time. This procedure quickly identified time varying correlator related problems quite effectively.

The output of the `table` and `closure` programs as a function of time were also saved in a file. This data was later examined and used to generate a flagging table readable by `AIPS`. These procedures, effectively generated first order on-line data flagging information, which is the crucial first step in improving the final data quality. Lack of time did not permit implementing these procedures as part of the on-line array control and correlator control software, but must be done in the near future to improve the reliability and quality of the final data.

## 4.4 Data Analysis

Two types of data analysis were required for mapping: (1) off-line data analysis (before and after importing the data into `AIPS`) for further, more careful identification of bad data, and (2) data analysis involving 3D inversion, deconvolution and phase calibration for the purpose of imaging. This section describes the procedure used for the data analysis required for data editing and calibration. Section 4.5 describes the procedure used for mapping.

### 4.4.1 Data Editing

In addition to the data flagging information derived from on-line system and data monitoring, the data was also examined off-line using the programs `xtract`, `rantsol` and `badbase` (see Chapter 3). In long observing sessions, there were invariably antennas which did not produce usable signals for some fraction of time. Often, this was either due to th malfunctioning of a subsystem or the antenna being taken for some kind of maintenance work over time scale much longer than the threshold time intervals set in the on-line monitoring programs (see Section 4.3.1). Such situations were easily identified from the plots of amplitude from all baselines (or for all baselines with a single antenna) as a function of time for the calibrator scans. The calibbp program was also used for bandpass calibration of the data, using the phase calibrator scans. The antenna-based average bandpass solutions and the baseline based band-passes were examined to identify frequency channels affected by intermittent narrow band RFI or by any other source of data corruption.

The program badbase uses the output of rantsol to generate a summary of the antenna based solutions (see section 3.5.2, Chapter 3). This was found to be very useful in identifying intermittent baseline based problems in the data. The AIPS tasks used for calibration are rather sensitive to the presence of bad baselines in the data. Flagging data corrupted by baseline based errors was therefore essential. The algorithm for the computation of antenna based complex gains implemented in rantsol is robust in the presence of such data and was hence crucial for the identification and flagging of such data.

The above mentioned procedure was followed for data from both the polarization channels separately. All the flagging information generated from on-line monitoring and off-line data analysis, was converted to flagging tables to be used later for flagging data in AIPS.

Data recorded in the native LTA format was imported to AIPS via the FITS format. The program gl2fit was used to convert the LTA database into FITS format. It was noticed that data for some of the baselines was in the illegal number representation identified as NaN (not-a-number) or Inf (infinite) numbers. Most of the data analysis programs (including the robust algorithm of rantsol) behave erratically in the presence of such numbers. However, computer representation of such numbers is well documented in the IEEE number representation format and can be easily and reliably identified in the software. This form of bad data was therefore removed using an on-the-fly filter used in all off-line data analysis programs, including gl2fit. Another form of bad data manifests itself in the form of the normalized visibility amplitude being greater than unity. This is again easily identified in the software, and the gl2fit program flags such data while converting it to the FITS format.

Due to synchronization problems between the various network programs of the GMRT data acquisition software and the online array control software, the time stamp of the data records is sometimes corrupted and the value of time stamp of the successive data records does not increase monotonically. Data with such time stamp corruption is unusable in AIPS. Also, a few data records at the beginning of each scan were found to be regularly bad. All such data records were filtered out using the program `tmac`. `tmac` was used as a data filter in a data pipe-line, before the program `gl2fit`. If the observation was split into a number of LTA files, the program `ltacat` was also used before `tmac` in the data pipe-line to concatenate the various LTA files into one file. LTA files for some observations also required changing the values of some of the keywords in the Global an Scan headers of the LTA data base. This was done using the program `fixit`.

A typical data pipe-line set up to convert the and LTA file to FITS format was therefore, [ltacat]⇒ [fixit]⇒ tmac⇒ gl2fit, where '⇒' indicates the flow of data and the parenthesis are used to indicate that the program were used only if necessary. Use of UNIX pipes eliminated the necessity of saving the intermediate LTA files, which would otherwise have required several giga bytes of disk space.

Further data editing was done after importing the data into AIPS. The bad data/ antennas/ baselines identified earlier were translated to AIPS readable flagging files and applied inside AIPS. Various steps used for further data editing and calibration inside AIPS are described below.

### 4.4.2 Data Editing and Calibration in AIPS

The first step in the sequence of data analysis is the amplitude and phase calibration of the visibilities. This section describes, in a stepwise fashion, the sequence of various AIPS tasks that were used for data calibration. A typical AIPS task depends on a large number of parameters, which control the behavior of the tasks. The settings of the relevant parameters of these tasks are also discussed below.

1. The FITS file generated using the procedure described above, was imported into AIPS using the task FITLD. This results into a multi-source visibility database written in AIPS, by default in the compressed format.

2. Normally, multi-source file contains a number of tables, including the CL table, version 1 (CL1)

   At present, the CL1 table is not generated when the GMRT data is converted into FITS format. This table is also used by AIPS calibration programs as a template to determine the time resolution for the subsequent CL and antenna gain tables (the

SN tables). Hence, the task INDXR was always run to generate the table CL1. This also generates the NX table, which is used by AIPS to navigate in the database. This, by default, produces a CL table with a time resolution of 5 min. Since the phase calibrators used for all the observations were strong enough to provide sufficient signal to noise ratio, the antenna based gain solutions could be computed for every integration cycle of $\sim 17$ sec. The CL and SN tables were later used to not only calibrate the data but also identify bad data. The minimum time resolution for gain solutions was therefore set to $\sim 20$ sec by setting APARM=0.33,0 before running INDXR.

3. The flux density for the flux calibrators must be accurately set before proceeding for calibration. The flux density scale of the standard VLA flux calibrators 3C48 and 3C286 is encoded in the task SETJY. This task was run on the multi-source visibility database to set the flux densities for these flux density calibrators using the following settings: OPCODE='calc'; SOURCE='3C286','3C48',''.

4. The task UVFLG reads the data flagging information from a disk file supplied via the INFILE keyword. This task was used to apply all the flagging information generated from the on-line monitoring and off-line data analysis described earlier.

5. The visibility amplitude of an unresolved source remains constant as a function of baseline length. Plot of visibility amplitudes as a function of $\sqrt{u^2 + v^2}$ for the flux density calibrator scans was examined using the task UVPLT. The SOURCE keyword was appropriately set for the purpose. Obviously discrepant data were identified, after allowing for some spread due to differences in antenna sensitivities. Such data, which either had very low or very high amplitude can have severe repercussions for calibration.

   UVFLG was used to flag these discrepant points with INFILE=''. The keywords ANTENNA, BASELINE, and TIMERANGE were used to specify the offending antennas/baselines and any time range for which the data was required to be flagged.

   The primary task for calibration in AIPS is CALIB. This task is, however, rather sensitive to the presence of bad/dead antennas. (e.g., in one case (G356.3-1.5) the presence of about 10 bad baselines out of a total of about ~360 good baselines (for antennas C06 and C05) gave severely under estimated antenna gains). The initial effort outside AIPS to identify and flag bad data/baselines paid good dividends at this stage of processing.

6. In some cases, the graphical flagging task TVFLG was also used to interactively flag bad data.

7. CALIB was then used to compute the antenna based complex gains for the flux density calibrator scans with SNVER=0, GAINUSE=0, SOLINT=0.33. This generates the first antenna gains table (SN1) containing complex gain solutions with a time resolution of $\sim 20$ sec.

8. To further identify bad data, the data was examined using UVPLT and VPLOT with DOCALIB=1 and SNVER=1. With these settings, the SN1 table is applied to the data on-the-fly. This essentially takes care of any short term variations in the antenna gains as well as variations in the sensitivity of the antennas.

   This procedure helps in identifying mildly discrepant data, which cannot be corrected by any antenna based correction. As before, UVFLG was used to flag such data. SN1 was then deleted using the task EXTDEST with INEXT='SN' and INVERS=0. This deletes the latest SN table generated in any previous run of CALIB. Steps 5 to 8 were repeated till a satisfactory SN1 table was generated for the flux density calibrator.

9. The task CLCAL was then used with INTERPOL = 'MWF'; INTPARM = 0.5,0.5; CALSOURCE = '3C286','3C48',''; SOURCE = '' to generate the second version of CL table (CL2) containing the median window filtered solutions derived from SN1. The resulting table CL2 contains flux calibration for *all* sources in the database and constitutes the basic flux calibration table.

10. Steps 5 to 9 were repeated for each phase calibrator to identify and flag bad data. This resulted into the third CL table (CL3) containing the median window filter solutions for the antenna gains, derived from the phase calibrator scans; this was used later to correct for slow variations in the antenna based complex gains.

    A fourth CL table (CL4) was also generated containing the the gain solutions for the phase calibrator with a time resolution of $\sim 20$ sec (INERPOL='2PT'). This was later used for band pass calibration.

11. GETJY was then used with CALSOURCE='3C286','3C48' and SOURCE='' to derive the flux density of the phase calibrator. If all was well in the above procedure, the derived flux density should be close to the value listed in the VLA calibrator manual and the error bars of less than 10% (after multiplication by the ratio of the sys-

tem temperatures for the flux and phase calibrator fields, since the GMRT visibility database as yet does not contain the $T^{sys}$ table). This corrects for the difference in the system temperatures between the flux and phase calibrators.

12. In all the above, a single, clean frequency channel, free from RFI, was used. All the calibrators used were strong enough to warrant the use of a single frequency channel. However, to use other channels for the purpose of imaging, a bandpass calibration also needs to be applied to calibrate any channel dependent gain variations.

    In the calibration procedure adopted here, it is assumed that the time calibration (determined in the above procedure) and bandpass calibration can be separated and determined independently. The time calibration table (`CL4`) was therefore applied to all the channels before deriving the band pass calibration table, the `BP` table. `AIPS` offers interpolation of the `BP` table in time to apply band pass calibration to data of the target source. Hence, the time calibrated data within the calibrator scans needs to be averaged, to generate a scan averaged band pass solution. The resulting band pass solutions (one per calibrator scan) can then be interpolated in time to take care of any slow variations in the band shape.

    However, data affected by intermittent RFI needs to be flagged before the data is averaged in time. RFI on calibrator scans was identified using the task `FLGIT` on these calibrator scans. This task examines the data after subtracting a linear fit to the band shapes from individual baselines. A user specified set of channels is used to determine the linear fit. All data with residuals outside the user specified limits are then flagged. All channels were flagged for a given integration time containing bad data. This was achieved with the following settings for `FLGIT`: `BCHAN=C0; ECHAN=C1; DOCALIB=1; GAINUSE=4` where, `C0` and `C1` are the first and the last frequency channels to be used. Several sets of `(C0, C1)` for range of clean frequency channels can be specified, which alone will be used for the linear fits, via the `NBOXES` and `BOX` keywords. The flagging criterion can be specified via the `APARM` keyword.

    `FLGIT` was also used later on the calibrated data on the target sources. However, since the signal to noise ratio on individual baselines for extended sources can vary a lot, such automated procedures are of limited use. Identification of bad data on the target source was therefore usually done manually using tasks like `UVPLT`, `UVFLG`, `TVFLG` and `SPFLG`.

13. The graphical data editing task SPFLG was sometimes used at this stage to identify and flag bad data. This task displays the data in the time-frequency plane from one baseline at a time and provides the same interface as that of TVFLG to graphically flag data.

14. Next, the BP table was derived by time averaging the data within the phase calibrator scans (after application of the time calibration). This was done using the task BPASS with DOCALIB=1; GAINUSE=4; BPASSPRM(5)=1; BCHAN=C0; ECHAN=C1 where C0 and C1 refer to the first and the last frequency channel to be used.

15. The BP table and band pass corrected band shapes were examined using the task POSSM. Large oscillations across the band were sometimes found in a few antennas. These antennas were usually flagged from the entire data base.

16. Finally, the task SPLIT was used to apply the time and band pass calibration (the CL and BP tables respectively) to the data on the phase calibrators as well as the data on the target source and single source multi channel calibrated databases generated. This was done using the following settings: DOCALIB=1; GAINUSE=3; DOBAND=3; BPVER=1.

**Flux density calibration**

Flux density calibration was done using observations of one of the two VLA flux density calibrators, 3C286 or 3C48. Time variability of these sources has been found to be small from the VLA monitoring of the flux densities of these sources. The absolute flux densities of these sources was derived by careful observations by Perley & Crane (1986) using the VLA in D-array configuration and they found that the Baars scale (Baars et al. 1977) was slightly in error. They adjusted the flux density of 3C295 to that of Baars value and derived corrections for the flux densities of 3C286 and 3C48. These corrected flux densities are encoded in the AIPS task SETJY which was used to set the flux densities for these sources used for flux density calibration. The adopted flux densities of 3C286 and 3C48 were $28$ and $42.7$ Jy respectively (at 325 MHz). Observations of 3C48 with the VLA has shown that the flux density derived using SETJY gives the 325-MHz flux density with an accuracy of $\sim 2$%.

The flux density calibrators were typically observed at the beginning and at the end of each observation. The phase calibrators used for these observations are also listed as good secondary VLA calibrators. The flux density calibrator scans were used to derive the flux densities of these secondary calibrators as a consistency check. The phase calibrators were also used as secondary calibrators to correct for any slow variations in the antenna gains. All fields observed for this dissertation also had many other sources in the field. For some of these sources, the 325-MHz flux densities were available from other independent observations as well (VLA calibrators, targeted VLA observations or the Texas survey (Douglas et al. 1996) which gives the spectral index and point source flux densities at 365 MHz). These flux densities were also used for a consistency check on the flux calibration and to eliminate the possibility of any systematic flux calibration error.

The background temperature in the Galactic plane can change quite substantially for separate pointings. For accurate flux density calibration, one must measure the system temperature for the flux density calibrator field as well as for the target field. To also account for small time dependent variations in the system temperature, it should be monitored regularly during the length of the observations. The planned periodic injection of calibrated noise at the front-end of each antenna to measure the system temperature has not yet been implemented at the GMRT. In its absence, the system temperature was measured at a few positions around the target source in the Galactic plane and the measured system temperature used to correct for the differences in the background temperature between the field of interest and the flux density calibrator. The background temperature from the 408-MHz all sky survey (Haslam et al. 1995) was also estimated as a consistency check. With this scheme, we estimate that the 325-MHz flux densities from GMRT are accurate to $\sim 15\%$.

**Phase calibration**

Slow variations of the antenna based complex gains occur on time scales of a few tens of minutes. The relative phase variations between the antennas due to this needs to be corrected so as to phase the array over several hours. These slow variations are measured using periodic observations of a phase calibrator. Since the system temperature at 325 MHz in the Galactic plane is a factor of 3-5 higher than away from the plane, the phase calibrators must also be strong (typically $> 10$ Jy) to provide enough signal to noise ratio for the computation of antenna based complex gains. Temporal as well spatial variations in the ionospheric total electron content at 325 MHz is expected to be the major source of phase corruption. This can produce phase variations over the scale of the array (and sometimes even across the primary beam of each antenna). It is therefore not advisable to use a phase calibrator too far from the target field since the antenna based complex gains obtained from the phase calibrator may not reflect the phase variations in the direction of the target field.

Using the antenna based phase variation derived from continuous observations of the phase calibrators for several hours (Figs. 2.11 and 2.12), it was estimated that phase variations over a time scale of about half an hour could be approximated well by linear interpolation. This is thus the time scale at which one needs to observe the phase calibrator ($\sim 30$ minutes). The three VLA 327 MHz calibrators `1709-299`, `1830-36`, and `1822-096` with 327-MHz flux densities of 6, 28, and 13 Jy respectively, were used as phase calibrators. The angular separation in the sky between the phase calibrators and the target field was typically $10 - 15°$. The maximum error in phase due to errors in the antenna coordinates, when the phases from the phase calibrator are transferred to the target source was estimated to be a few degrees (see Section 2.6.1). Tests done by phasing the data from one calibrator using periodic observations of another calibrator show that the array is phased over time scales of $\sim$half an hour using this procedure.

**Bandpass calibration**

The antenna based complex gains vary across the passband, primarily due to the antenna based band shape and residual fixed delay errors. These variations in the complex gains must be corrected before the visibilities from individual frequency channels are averaged.

As mentioned above, the phase calibrators were strong enough to provide enough signal to noise ratio for the computation of channel dependent antenna based complex gains. The antenna band shape corrections were therefore derived using the phase calibrators. An average gain was computed for each of the phase calibrator scans per channel and the linearly interpolated values applied to the target source data to correct for the channel dependent complex gains.

## 4.5 Inversion and deconvolution of GMRT data

The 325-MHz primary beam of GMRT antennas has a full width at half maximum (FWHM) of $\sim 1^\circ.4$. The central square provides a maximum baseline of $\approx 1$ km equivalent to an angular resolution of $\sim 3$ arcmin. At this resolution, the full GMRT primary beam can be mapped without severe degradation due to non-coplanar effects. As a first step, with the dual purpose of gauging the data quality and locating strong confusing sources, single facet images were made at a resolution of $\approx 1$ arcmin using the task IMAGR.

Having identified the sources in the field of view from this lower resolution image, higher resolution imaging was attempted. Typically, a maximum baseline of 20k$\lambda$ was used corresponding to an angular resolution of $\sim 15$ arcsec. Most of the fields had strong extended sources all over the field of view forcing the mapping of the full primary beam. At these resolutions, the number of planes required along the n-axis is 8. Hence, a 3D inversion was required. The IMAGR task of AIPS performs a 3D inversion using the polyhedron imaging algorithm. In this, the entire field of view is divided into a two dimensional grid of facets. A small part of the sky (corresponding to the size of the facet) centred around each facet is then imaged by first shifting the phase centre of the visibility to the centre of the facet and then performing the normal 2D inversion and CLEANing. Since, the 2D approximation is assumed to be valid within the facet, it is important to make sure that the facet is not so big as to re-introduce distortions at the edges of the facets.

The number of facets required for 3D inversion using IMAGR and the appropriate RA and DEC shifts for the centre of each facet, were computed using the relatively new task in AIPS called FCSET. Essentially, given the size of each facet, the size of the field of view and the RA and DEC of the phase center, this task writes out a IMAGR readable list of field specifications (the field number, its RA and DEC shifts and its size in number of pixels along the RA and DEC axis). Typically, this resulted in a $5 \times 5$ grid of facets, each of size $256 \times 256$.

After the inversion of each of the facets, the IMAGR task uses the usual 2D Clark CLEAN (Clark 1980) on each facet. The class of CLEAN and MEM based deconvolution algorithm treats each pixel in the image as a degree of freedom. Even when mapping in the Galactic plane (or close to it), it is clear from the images that most of the pixels do not have any physical emission associated with them. Reconstruction of the physical emission in the field of view should therefore be somehow constrained to use only those pixels where there is significant physical emission from the sky. Not doing so is equivalent to giving more freedom to a non-linear fitting process (the deconvolution process), than is justified by the data. CLEAN based algorithm (and its variants) are themselves unconstrained. This constraint must therefore be provided externally by setting boxes around the dominant sources in the field of view at each cycle of CLEAN. It has been shown by Briggs (1995) that the best results are obtained by putting as tight a box as justified by the data (essentially by inspection). During the deconvolution process, the IMAGR task provides a facility to dynamically define boxes for each field for every cycle of CLEAN.

However, since the emission was usually of complex morphology making it difficult to define tight boxes, simple square boxes enclosing the source of emission were used. This was manually done for each facet.

The resulting set of facet images were put together to reconstruct the sky using the task `FLATN`. The `FLATN`ed image was then primary beam corrected using the task `PBCOR`. The GMRT visibilities correspond to the date-epoch at the time of observations. The final image was therefore rotated to the J2000 epoch using the task `REGRD`.

## 4.6 The Images

This section presents the final images produced via the procedure described above. All images were corrected for primary beam attenuation using a polynomial approximation of the GMRT primary beam. As mentioned earlier, the resolution in these images changes from image to image due to a combination of declination dependent uv-coverage, changes in the number of available antennas and the flagging of bad data. Images of fields with large angular size sources are presented at a few arcmin resolution. Higher resolution images of some of the fields were also made where necessary (due to the presence of small angular size sources of interest in the field, e.g. the field containing G003.6-0.1).

Fig. 4.4 shows the GMRT image of the field containing the SNR G001.4-0.0 at the centre of the image. Other well known sources (SNRs and H II) regions in the Galactic Centre region are clearly visible in this image. The RMS noise is relatively high, possible due to the Galactic Center which lies at the south-western edge of the primary beam. Few of the GMRT antennas had servo related errors due to which there were small oscillations in the antenna pointing while tracking. This, in the presence of strong sources at the edge of the fields, results in short time scale differential gain variations which are not easy to correct later and also results in a higher RMS noise.

Fig. 4.5 shows the full primary beam corrected images of the field containing the SNRs G004.7-0.2, G003.8+0.3 and the unclassified source G003.6-0.1. The low resolution image in the left panel was made using a single facet, while the higher resolution image was made using a grid of $4 \times 4$ facets. The lower surface brightness SNR G003.8+0.3 is better discerned in the low resolution image.

The dominant extended source in Fig. 4.6 is a known Ultra Compact H II region (Becker et al. 1994). A small angular size SNR G004.2-0.0 was reported by Gray (1994a) in this field at the centre of this image. However there is no indication of this source at the level of

10 mJy/beam in this image. It is, however detected as a compact flat spectrum source in the low resolution image. This sources is unlikely to be an SNR.

Fig. 4.7 shows the GMRT 325-MHz image of the shell type SNR G004.8+6.2. The strong, marginally resolved source due west of this SNR is the well known Kepler's SNR (Fig. 5.14). G004.8+6.2 is again clearly detected in the NVSS image of this region (Fig. 5.7). This SNR is also detected in the image made from a 327-MHz VLA observation of a region close to this source (Fig. 5.8).

Fig. 4.8 shows the field containing the barrel shaped SNR G356.2-1.5. The 843-MHz image of this SNR by Gray (1994a) was severely affected by artifacts due to the grating response of nearby sources. This SNR is however clearly detected in the GMRT 325-MHz image. A marginally extended source of emission is also visible in this image in the north-eastern direction.

Fig. 4.9 shows the GMRT image of the shell type SNR G356.2+4.5. This SNR is also clearly visible in the NVSS image of this region (Fig. 5.10). The quality of NVSS images close the Galactic plane is usually poor. However, a few degrees away from the plane, low surface brightness SNRs are often easily visible in NVSS fields (Trushkin 1999; Bhatnagar 2000; Green 2001). A careful examination of the NVSS fields, few degrees away from the plane is therefore likely to result in the identification of more, hitherto unknown SNRs. Deep imaging of such objects can then be followed up with the GMRT/VLA. Detailed multi frequency imaging of a number of high Galactic latitude SNRs can be used to possibly deduce the distribution of ionized gas and examine the statistical significance of the $\Sigma$-$D$-$z$ relation (Caswell & Lerche 1979).

Fig. 4.10 shows the GMRT image of the incomplete shell of the SNR G358.0+3.8. This is a low surface brightness SNR, but also detected in the NVSS image (Fig. 5.11).

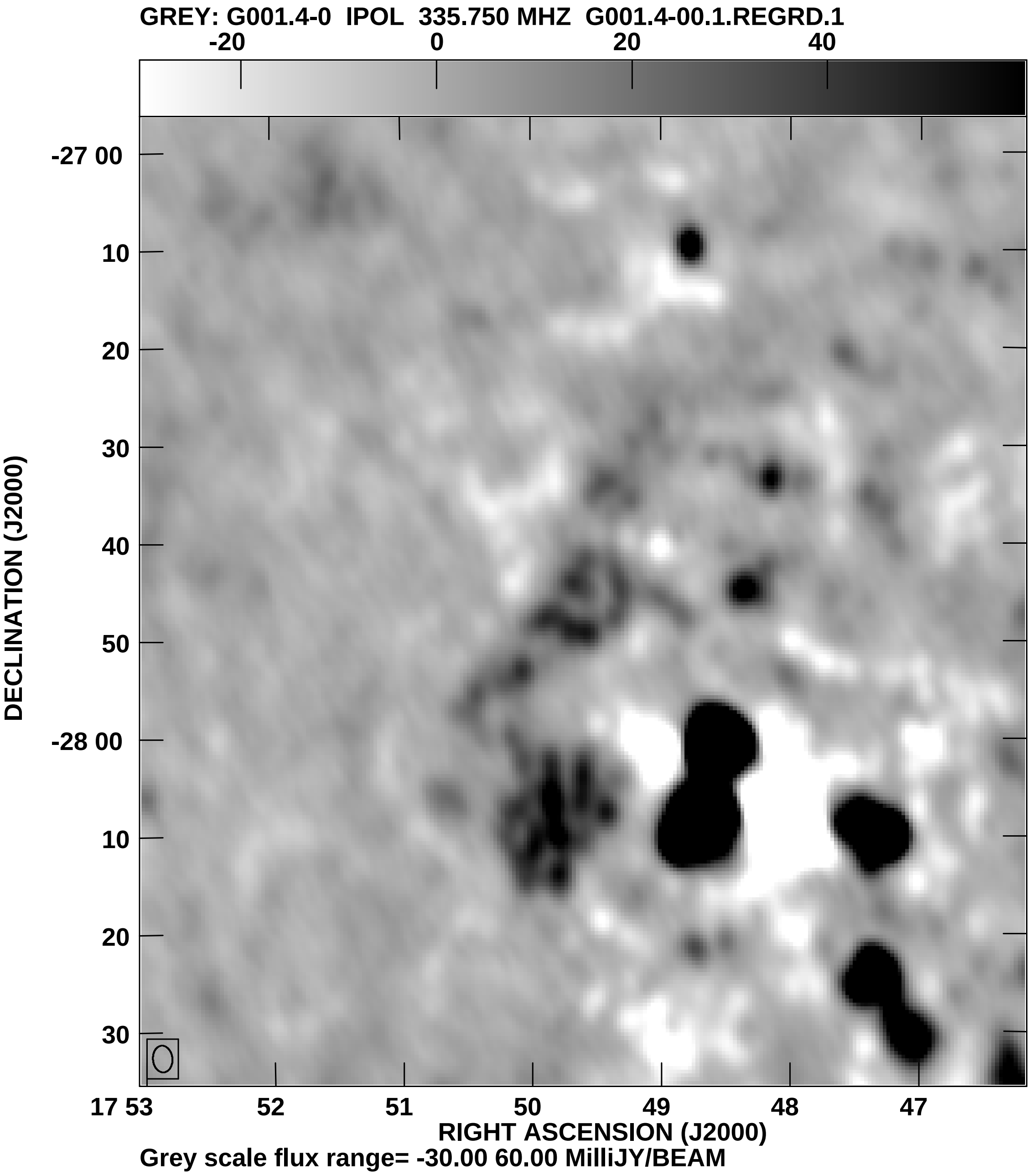


Figure 4.4: Full primary beam image of the field containing the sources G001.4−0.0 at the centre of the image. The resolution in the image is $\approx 3 \times 2\,\mathrm{arcmin}^2$. The RMS noise in the images is $\sim 30$ mJy/beam. The Galactic Centre sources (LaRosa et al. 2000) Sgr D HII region and Sgr D SNR pair, the SNR G000.9+0.1, Sgr B1 and Sgr B2 are the dominant sources in the south-east direction.

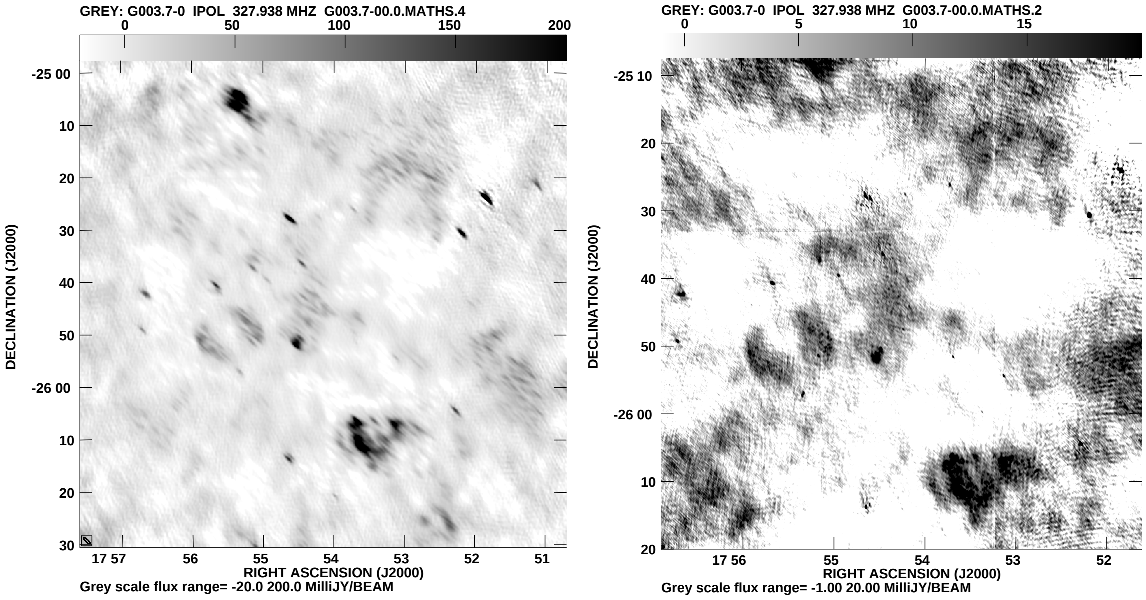


Figure 4.5: Full primary beam image of the field containing the sources G003.6−0.1, G003.7-0.2, and G003.8+0.3. The resolution in the image in the left panel is this image $\approx 98 \times 29\ \mathrm{arcsec}^2$ while that in the image in the right panel is $\approx 20 \times 11\ \mathrm{arcsec}^2$. The RMS noise in the images is $\sim 5$ mJy/beam. The extended emission is more clearly visible in the low resolution image, which was generated using a single facet. The higher resolution image was made with multiple facets.

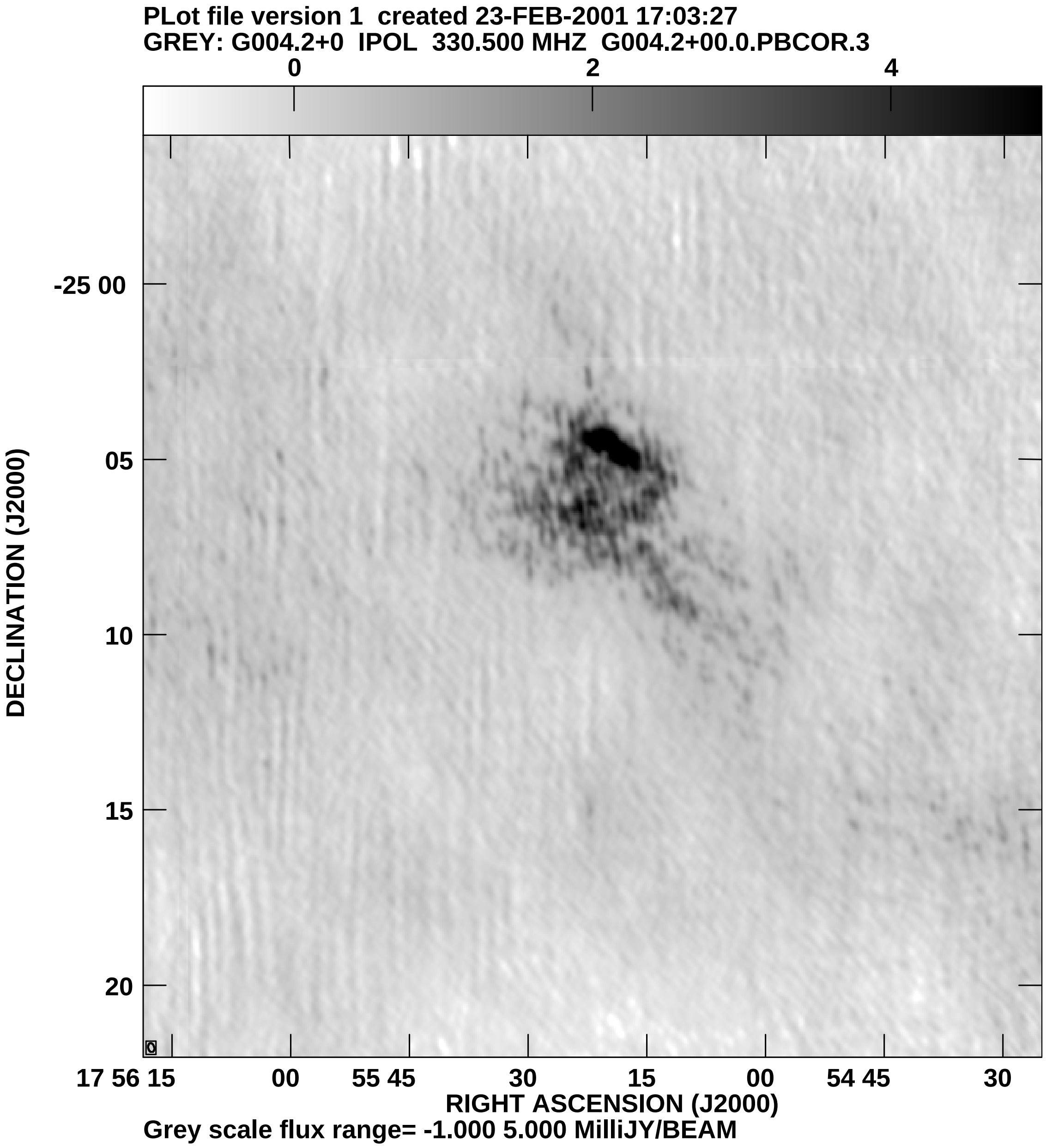


Figure 4.6: High resolution, multi facet image of the field containing G004.2−0.0. The resolution in the images is $\approx 15 \times 10$ $\mathrm{arcsec}^2$ and the RMS noise $\approx 5$ mJy/beam. The dominant extended source in the field is an Ultra Compact H II region. There is a hint of a emission at the location of G004.2−0.0, but much below the expected level, probably indicative of thermal source (see Figure 5.5 for a low resolution image where G004.2−0.0 is detected as compact source).

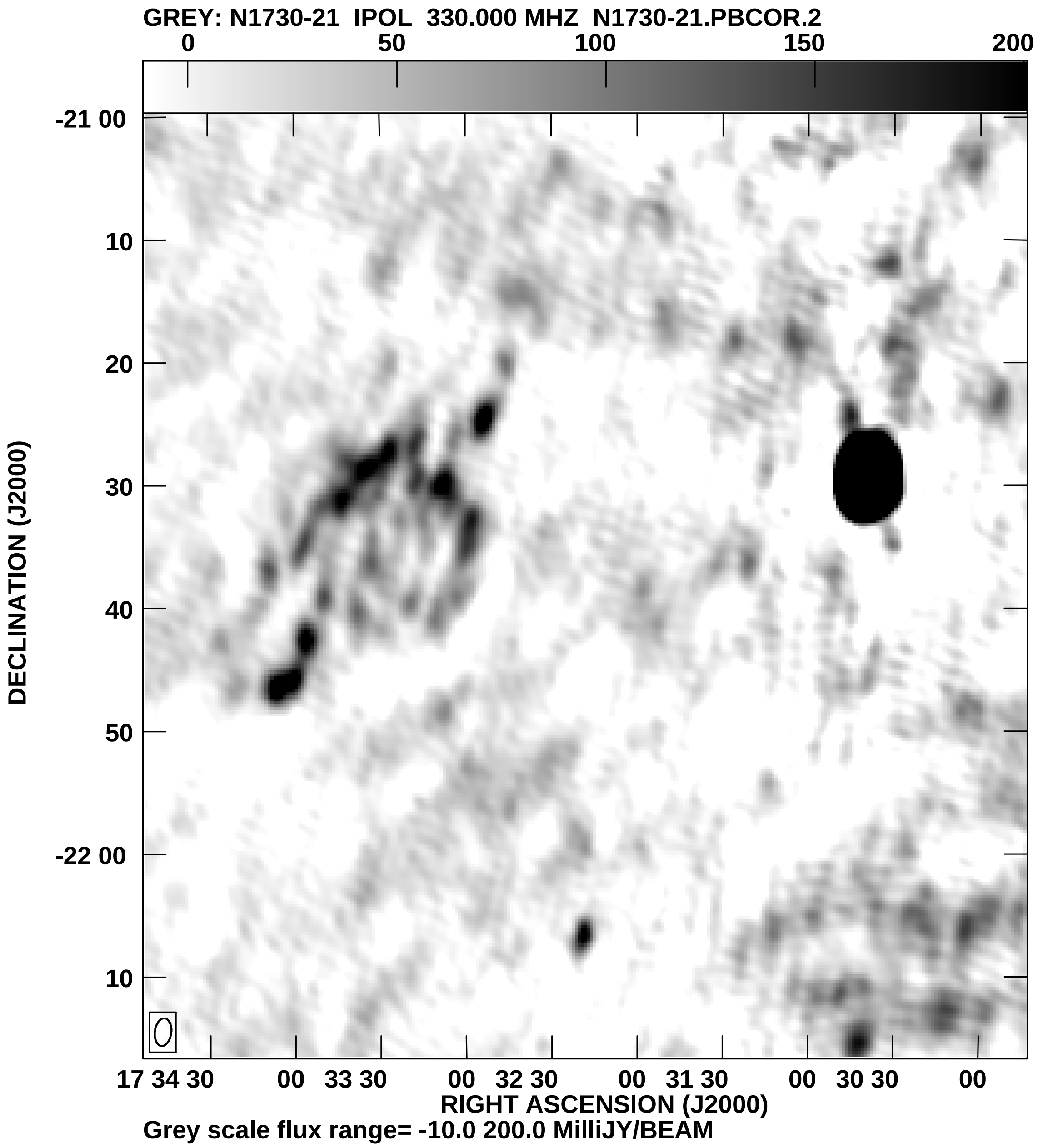


Figure 4.7: Full primary beam corrected image of the field containing G004.8+6.2. The weaker source, due east of the centre of the image is the SNR G004.8+6.2. The strong source due west of the image centre is the 38 Jy Kepler's SNR. The resolution in the image $\approx 2.3 \times 1.4~\mathrm{arcmin}^2$ and the RMS noise is $\approx 23$ mJy/beam. Apart from other unknown sources of noise, the higher RMS noise in this image is also due to the wobble in the antenna pointing for some of the antennas used for this observation.

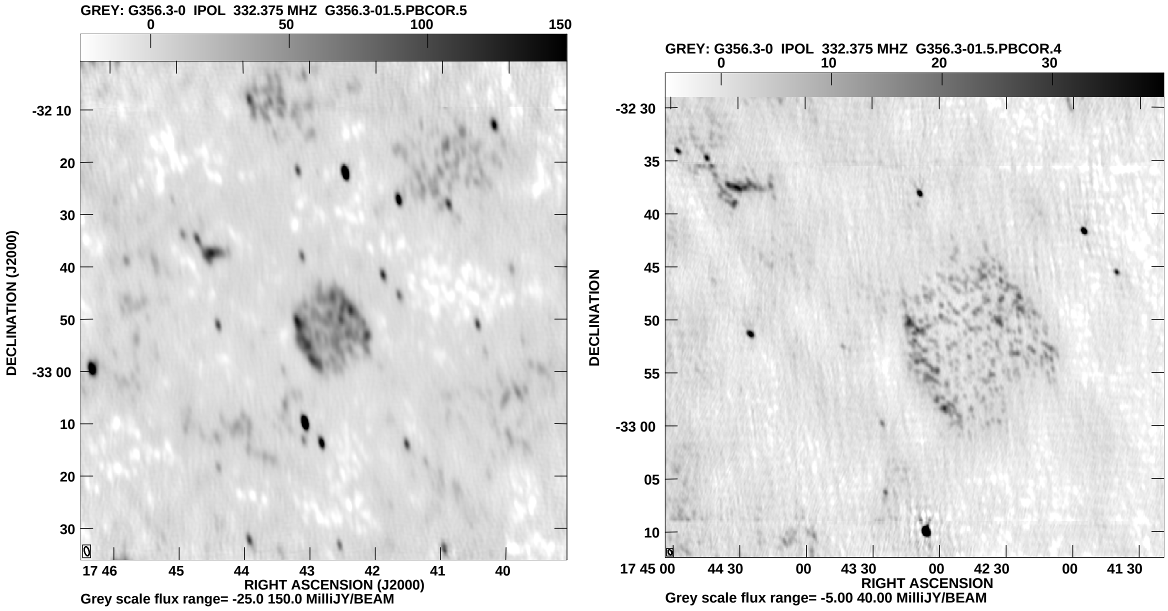


Figure 4.8: Multi facet image of the field containing G356.2-1.5. The resolution in the image on the left is $\approx 1.7 \times 0.8\ \mathrm{arcmin}^2$ and the RMS noise is $\approx 5$ mJy/beam. Notice the extended emission north-east of the barrel shaped SNR in the centre of the field. The panel on the right shows a high resolution image of this extended source.

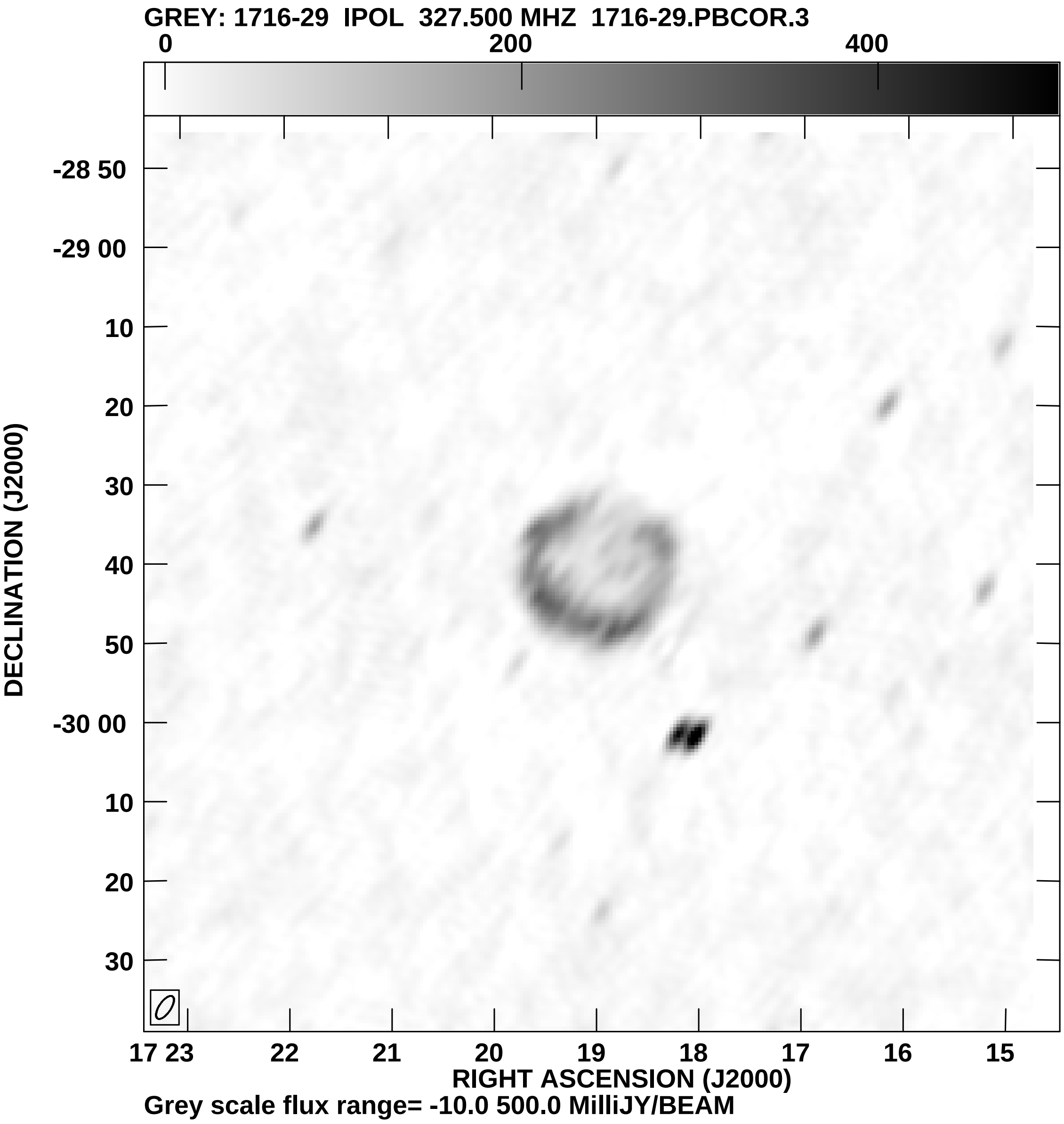


Figure 4.9: Full primary beam corrected image of the field containing G356.2+4.5. The resolution in the image is $\approx 3 \times 1.5\ \mathrm{arcmin}^2$ and the RMS noise is $\approx 10$ mJy/beam.

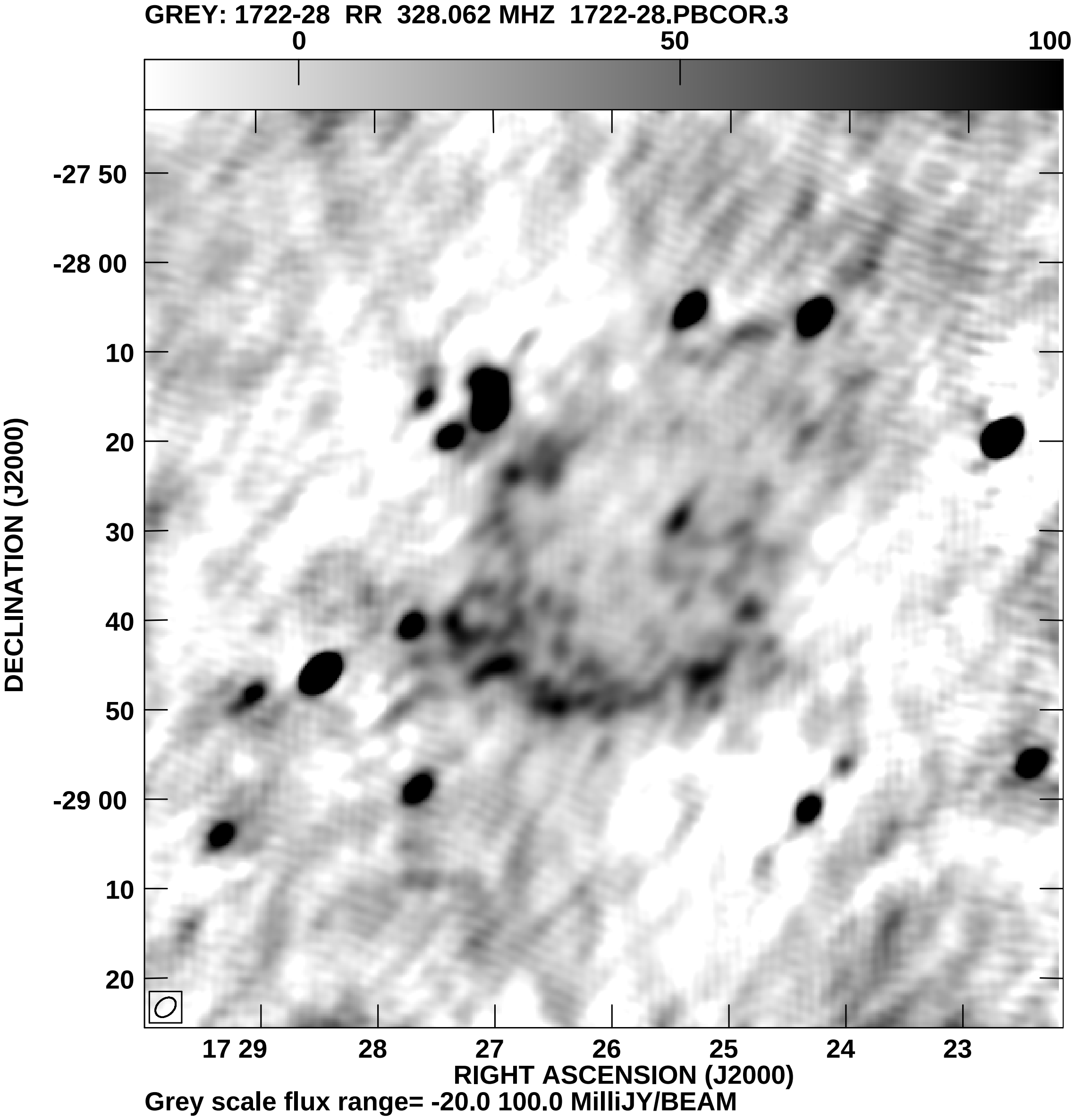


Figure 4.10: Full primary beam corrected image of the field containing G358.0+3.8. The resolution in the image is $\approx 2.6 \times 1.5\ \mathrm{arcmin}^2$ and the RMS noise is $\approx 15$ mJy/beam.